




## The High-Frequency Decay Parameter ( $\kappa$ ) in Taiwan

SHUN-CHIANG CHANG,<sup>1</sup> KUO-LIANG WEN,<sup>2</sup>  MING-WEY HUANG,<sup>3</sup> CHUN-HSIANG KUO,<sup>4</sup> CHE-MIN LIN,<sup>4</sup>  
CHUN-TE CHEN,<sup>5</sup> and JYUN-YAN HUANG<sup>4</sup>

**Abstract**—The high-frequency decay parameter  $\kappa$  was computed by fitting Fourier amplitude spectra from the seismic network of the Taiwan Strong Motion Instrumentation Program (TSMIP). The  $\kappa$  of shear horizontal waves (SH waves) was calculated for individual recordings, and the relationship between  $\kappa$  values and the epicentral distance ( $R_{\text{epi}}$ ) of each station was derived for each station. The  $\kappa$  value at  $R_{\text{epi}} = 0$  (denoted as  $\kappa_0$ ) can be used as a site parameter. There are totally 26,277 seismograms that have been recorded at 679 TSMIP stations over the period of 1993 through 2014 with local magnitudes of 4.0–7.1 and focal depths less than 30 km. The estimation of  $\kappa_0$  for Taiwan ranges from 0.0208 to 0.147 s, and the spatial distribution of  $\kappa_0$  was closely related to geology and velocity. The site-specific  $\kappa_0$  values from 425 stations were correlated with the averaged shear wave velocity of the top 30 m of strata ( $V_{S30}$ ), and the relationship could be described as  $\kappa_0 = (0.125 \pm 0.005) - (0.011 \pm 0.001) \times \ln(V_{S30})$ , and an acceptable linear correlation ( $R^2 = 0.57$ ) was performed. The results may be used in the future application of ground motion prediction equations (GPMs) and serve as simulation parameters. Also, the relationship between  $\kappa_0$  and the depth to engineering rock ( $Z_{1.0}$ ) is not well correlated, whereas an acceptable correlation exists between  $\kappa_0$  and other site proxies (i.e., elevation and resonant frequency).

**Key words:** Site effects, decay parameters,  $\kappa$ ,  $V_{S30}$ ,  $Z_{1.0}$ .

### 1. Introduction

Taiwan is located at the convergent boundary of the Philippine Sea Plate and the Eurasia Plate. The country thus has dozens of onshore active faults and experiences high seismicity (Fig. 1). Many of the disastrous large earthquakes that have occurred in Taiwan are associated with local site effects (Tsai et al. 2001; Wen et al. 2008), which have an enormous influence on the intensity and characteristics of ground motion. An influential investigation of the role of site effects was carried out by Boore and Joyner (1997) which incorporated the frequency-dependent amplification function with frequency-independent attenuation for five site conditions. They found that seismic waves are amplified when they propagate through the low-shear-velocity and low-density layers, while the shallow structure can cause attenuation at the same time. In their calculation, attenuation was assumed to be frequency-independent, which is known as the spectral decay parameter (denoted as  $\kappa_r$ ).

Exponential decay of the acceleration Fourier amplitude spectrum will occur above a specific frequency (hereafter denoted as  $f_E$ ). Anderson and Hough (1984) defined exponential decay at the high frequency of the spectrum as  $\sim A_0 \exp(-\kappa_{r\_AS} \pi f)$ , where  $A_0$  and  $f$  are the spectra amplitude and the frequency in Hz, respectively. The authors also stated that  $\kappa_{r\_AS}$  was related to epicentral distance ( $R_{\text{epi}}$ ), expressed as  $\kappa_{r\_AS} = m_\kappa \times R_{\text{epi}} + \kappa_{0\_AS}$ , where  $\kappa_{r\_AS}(\kappa_r)$  is high-frequency decay of the S wave Fourier spectrum,  $m_\kappa$  is the anelastic effect of the regional geological structure and  $\kappa_{0\_AS}(\kappa_0)$  is the site-dependent value. Furthermore, they suggested that  $\kappa_{0\_AS}$  may represent the attenuation of seismic waves in the first few hundred meters to kilometers beneath

<sup>1</sup> Sinotech Engineering Consultant, LTD, Taipei, Taiwan, ROC. E-mail: scchang@mail.sinotech.com.tw

<sup>2</sup> Department of Earth Sciences, National Central University, Chungli, Taiwan, ROC. E-mail: wenkl@cc.ncu.edu.tw

<sup>3</sup> National Science and Technology Center for Disaster Reduction, New Taipei City, Taiwan, ROC. E-mail: mwhuang@ncdr.nat.gov.tw

<sup>4</sup> National Center for Research on Earthquake Engineering, Taipei, Taiwan, ROC. E-mail: chkuo@ncree.narl.org.tw; cmlin@ncree.narl.org.tw; jyhuang@narlabs.org.tw

<sup>5</sup> Institute of Earth Sciences, Academia Sinica, Taipei, Taiwan, ROC. E-mail: pokayoke69@gmail.com

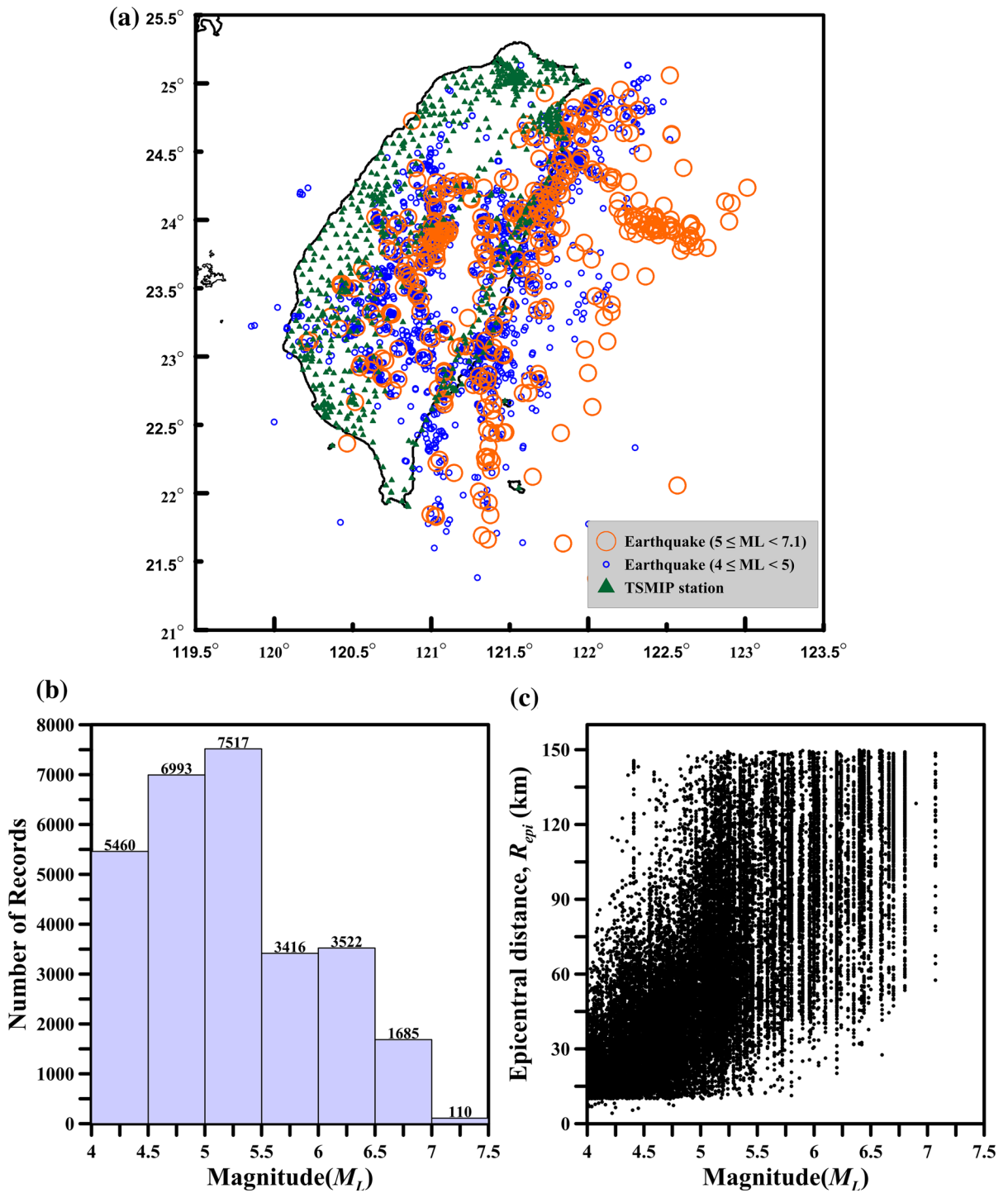


Figure 1

**a** Map of the TSMIP stations and epicenters of the earthquake events used in this study, **b** number of records and  $M_L$  distribution of the events, and **c** distribution of the magnitude ( $M_L$ ) and the epicentral distance ( $R_{epi}$ ) of the selected records

the site, depending on geotechnical site characteristics (Anderson and Hough 1984).

The  $\kappa_{0\_AS}$  value can be treated as an effect of the near-surface attenuation parameter when  $R_{epi}=0$  (Hassani and Atkinson 2018); this measure has recently been used in engineering and seismological applications. A number of studies have also used  $\kappa_{0\_AS}$  to describe intrinsic high-frequency attenuation while computing theoretical site amplification (Huang et al. 2005, 2007) to control the spectral shape of synthetic accelerograms generated with stochastic methods in ground motion simulations (Beresnev and Atkinson 1997, 1998; Boore 2003; Sokolov et al. 2004; Graves and Pitarka 2010; Mai et al. 2010). It can also be used as an adjustment factor in ground motion prediction equations (GMPEs) to improve the ground motion prediction from earthquakes at a specific location (Toro et al. 1997; Cotton et al. 2006; Campbell 2003; Atkinson and Boore 2006; Douglas et al. 2006; Edwards et al. 2011; Laurendeau et al. 2013; Al Atik et al. 2014; Baltay and Hanks 2014; Van Houtte et al. 2014; Zandieh et al. 2016).

In Taiwan, Tsai and Chen (2000) used accelerograms observed at stations of the Strong Motion Array Taiwan (SMART 1 array) to obtain an estimate of  $f_E$  and  $\kappa_{0\_AS}$  of the station in Ilan county, northeastern Taiwan. Van Houtte et al. (2011) used a total of 6 events and 99 records for analysis at 27 stations which are located either on stiff soil or rock, with a resulting  $\kappa_{0\_AS}$  value of around 0.05 s for the Taiwan region. Chen et al. (2013) used a total of 90 events recorded at 26 stations with either soil or rock conditions from 1995 to 1997 to estimate  $\kappa_{0\_AS}$  value distribution in the Kaoping area in southwestern Taiwan.  $\kappa_0$ s varies in the range of 0.06–0.12 s. Huang et al. (2017) used a total of 85 events recorded at 54 stations located on rock, very dense soil and soft rock, stiff soils, and soft soils from 1993 to 2010 to estimate  $\kappa_{0\_AS}$  values ranging from 0.034 to 0.066 s in the Taipei basin. The abovementioned studies only investigated the  $\kappa_{r\_AS}$  values in the specific region as well as the average  $\kappa_0$  values for the Taiwan region. Lai et al. (2016) determined  $\kappa_{0\_AS}$  values in Taiwan from 30 borehole seismic arrays containing force balance accelerometers (FBAs) at the surface and in the borehole. The resulting  $\kappa_{0\_AS}$  values are in the

range of 0.032–0.097 s at the surface and 0.012–0.078 s in boreholes.

In this paper, we computed  $\kappa_r$  from 26,277 seismograms in Taiwan. Firstly,  $\kappa_r$  was measured from the shear horizontal wave (SH wave) windows, and site-specific  $\kappa_0$  values were computed by removing the regional anelastic effect. Secondly, we investigated the relationship between  $\kappa_0$  and the average shear wave velocity of the top 30 m of strata ( $V_{S30}$ ), engineering application depths for  $V_S = 1.0$  km/s ( $Z_{1.0}$ ), station elevation and resonant frequency.

## 2. Strong Motion Data

The seismic network of the Taiwan Strong Motion Instrumentation Program (TSMIP), which is operated by the Central Weather Bureau (CWB), collects high-quality instrumental ground motion recordings. Every TSMIP station is equipped with tri-axial FBAs, which have a flat frequency instrumental response from direct current (DC) to about 50.0 Hz. Further details regarding the network are described in Liu et al. (1994). All stations are named according to their location and are grouped into eight areas: the Taipei Basin (TAP), the Taichung area (TCU), the Chiayi and Tainan area (CHY), the Kaohsiung and the Pingtung areas (KAU), the Taitung area (TTN), the Hualien area (HWA), the Ilan area (ILA), and the Free-field Strong Motion Network in the Taiwan Mountain Area (MTN). The free-field stations are spaced approximately 5 km apart, whereas the urban stations are only about 3 km apart. In total, 679 stations were in use during the study period, including 425 stations with  $V_{S30}$  data from the Engineering Geological Database for TSMIP (EGDT; Kuo et al. 2012). Figure 1 shows the locations of the 679 TSMIP stations overlaid with the earthquake events selected for use in this study.

The seismograms from earthquakes with local magnitudes ( $M_L$ ) of 4.0–7.1 and a focal depth of less than 30 km that occurred between 1993 and 2014 were selected to measure  $\kappa_r$  (Shin et al. 2013). A total of 26,277 digital accelerograms from 2204 earthquakes with an  $R_{epi}$  of 0–150 km were used. And in order to reduce the possibility of nonlinear effects, only the  $PGA < 50$  record is used. We excluded data

from the  $M_W$  7.6, Chi-Chi, Taiwan earthquake in 1999, due to difficulties in using its complicated source rupture (which extended 100 km along Che-lungpu fault) in interpreting the ground motion observations (Ma et al. 2001).

### 3. Methods of Measurement

Anderson and Hough (1984) stated that high-frequency decay of the acceleration spectral amplitude above a specific frequency ( $f_E$ ), which is definitively larger than the corner frequency ( $f_c$ ), can be described by the following equation [similar to Cormier (1982)]:

$$A(f) = A_0 e^{-\pi\kappa_r f} > f_E, \quad (1)$$

where  $\kappa_r$  is the spectral decay parameter, and is controlled by attenuation along the path and site;  $A_0$  depends on both the source,  $R_{epi}$  and site condition; and  $f_E$  is the frequency above which the spectral amplitudes decay exponentially.

Seismic recordings are usually in accordance with the geographical coordinate, i.e., east–west (EW), north–south (NS), and vertical-to-earth directions. However, earthquakes occur from different orientations, so there could be directional problems with this classification. According to rotation equation (Lay and Wallace 1995), the horizontal couples of EW and NS seismograms can be transferred to the radial and tangential couples ( $R$  and  $T$  component) as follows:

$$\begin{bmatrix} U_\theta \\ U_\phi \end{bmatrix} = \begin{bmatrix} -\sin(\phi_b) & -\cos(\phi_b) \\ \cos(\phi_b) & -\sin(\phi_b) \end{bmatrix} \begin{bmatrix} U_{EW} \\ U_{NS} \end{bmatrix} \quad (2)$$

$U_{EW}$  and  $U_{NS}$  represent the east–west and north–south seismic records;  $\phi_b$  is the back azimuthal angle of the station with respect to the earthquake source; and  $U_\theta$  and  $U_\phi$  are the radial and tangential seismic records, respectively. To measure  $\kappa_r$  from the selected recordings, the acceleration spectra were calculated from fast Fourier transform technique on SH wave windows for the  $T$  component. According to Tsai and Chen (2000), the time window length has little influence on the determination of  $\kappa_r$ , as long as the selected time window incorporates the strong energetic part of the shear wave. The arrival and end times of the SH waves were manually determined,

and each recording was visually inspected to ensure that the SH wave windows in the time series were correctly selected. The recordings used were previously corrected with the baseline subtraction of the average of all points in the recording. The beginning and end of the time windows were 5% Hanning-tapered.

$\kappa_r$  can be computed by a linear least-squares fit to the amplitude spectra at high frequencies. The logarithmic spectral amplitudes begin to decrease linearly with frequency, commencing at  $f_E$  and ending at  $f_X$ . The  $f_E$  points for each component were visually identified and manually selected;  $f_X$  points were selected using an automated method detailed below. In order to limit the impact of the source effect on the measurement of  $\kappa_r$ ,  $f_E$  should be higher than the corner frequency ( $f_c$ ). The  $f_c$  of  $M > 5$  is generally lower than 2 Hz (Castro and Avila-Barrientos 2015), and the  $f_c$  of  $3.4 < M < 5.3$  is generally between 1 and 6 Hz (Douglas et al. 2010), so we only analyzed the events of  $M_L$  greater than 4, and we further checked the relationship between the  $f_E$  values and magnitude to ensure  $f_E$  exceeds  $f_c$  even for moderate events (cf. Fig. 4). On the other hand, to reduce the impact of site effects,  $f_E$  should be greater than the resonant frequency ( $f_r$ ; Parolai and Bindi 2004). The  $f_r$  value is derived via the average horizontal-to-vertical spectral ratio (HVSr) of the microtremor measurement (Huang 2009). Figure 2a shows an example of the acceleration seismograms of the east–west components (EW-COMP), north–south components (NS-COMP), SH components (SH-COMP) and SV components (SV-COMP) at station HWA002 during an  $M_L$  4.7 earthquake. Figure 2b displays the selection of  $f_E$  and  $f_X$  on the Fourier amplitude spectrum of the SH and SV wave. The red line is the averaged spectral amplitude over the frequency of 50–100 Hz (due to the Nyquist frequency equals 100 Hz) representing the background noise or the flat instrumental response.  $f_X$  is selected as the frequency corresponding to the last point where the spectral amplitude is above the regression line. And the frequency range  $\Delta f = f_E - f_X$  must be greater than 10 Hz. In addition, the signal-to-noise ratio is set to be at least 3, while the averaged spectral amplitude (the red line) is higher than the pre- $P$  waves-spectral amplitudes (displayed by a grey line). The

dependence of  $f_E$  on earthquake source and distance is presented in later sections. Lastly, we calculated the linear least-squares fit of the observed acceleration spectra in log-linear space. The  $\kappa_r$  value can be calculated from the slope using the following equation:

$$\kappa_r = \frac{-b}{\pi} \quad (3)$$

where  $b$  is the slope of the resulting linear fit. The error associated with the  $\kappa_r$  estimate depended on how well the high-frequency amplitude decay followed a linear trend. Theoretically, the rotated seismograms from the EW–NS coordinate to the  $R$ – $T$  one would diminish/eliminate the interference from the converted  $P$  wave on SH wave arrival of the  $T$  component while propagating through different media. The SH wave of the  $T$  component is less susceptible to interference from other waves, but the SV wave may be affected by the  $P$  wave; thus, the SH wave may show the characteristics of  $S$  waves. In Fig. 2b, the  $S$  wave windows from the  $T$  component and those from the  $R$  component are selected to measure the  $\kappa_r$  values. The selected  $f_E$  are 16 Hz and 14 Hz for the SH wave and for the SV wave, respectively. The  $\kappa_r$  values from the SH and SV waves are 0.052 s and 0.042 s, respectively, which implies the different frequency contents in these two kinds of wave arrivals. In this study, we only use the SH wave of the  $T$  component to estimate the  $\kappa_r$  value to characterize the frequency-independent parameter.

#### 4. Data Analysis

##### 4.1. Dependence of $f_E$ on Source and Distance

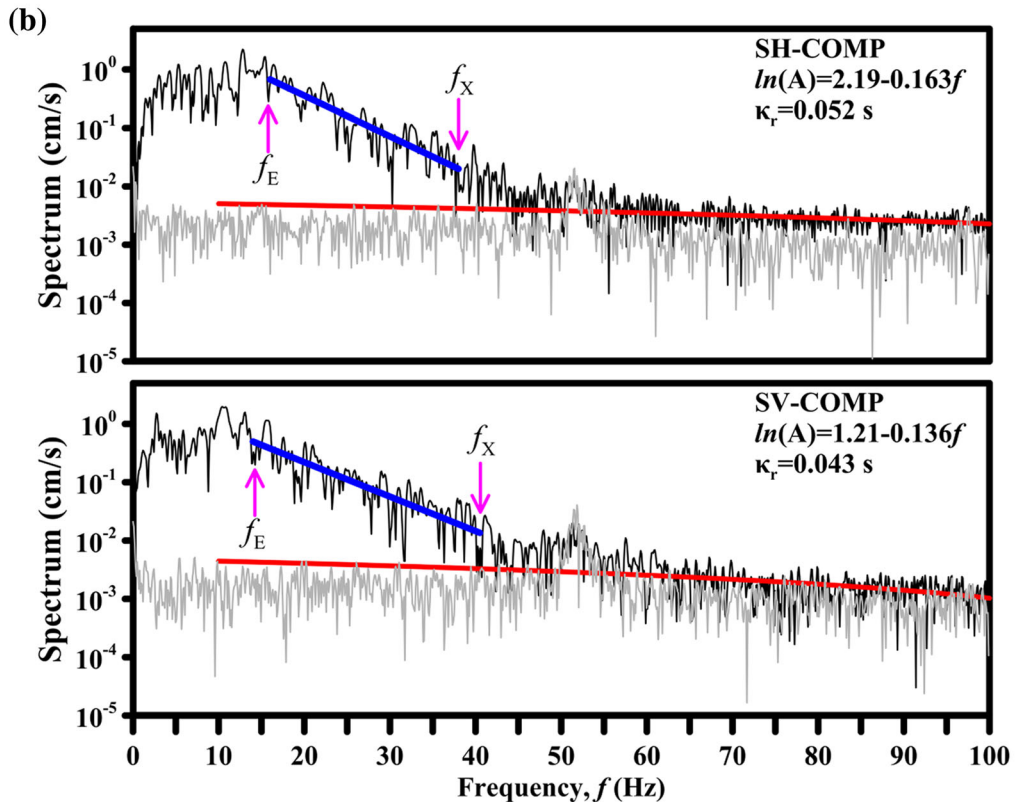
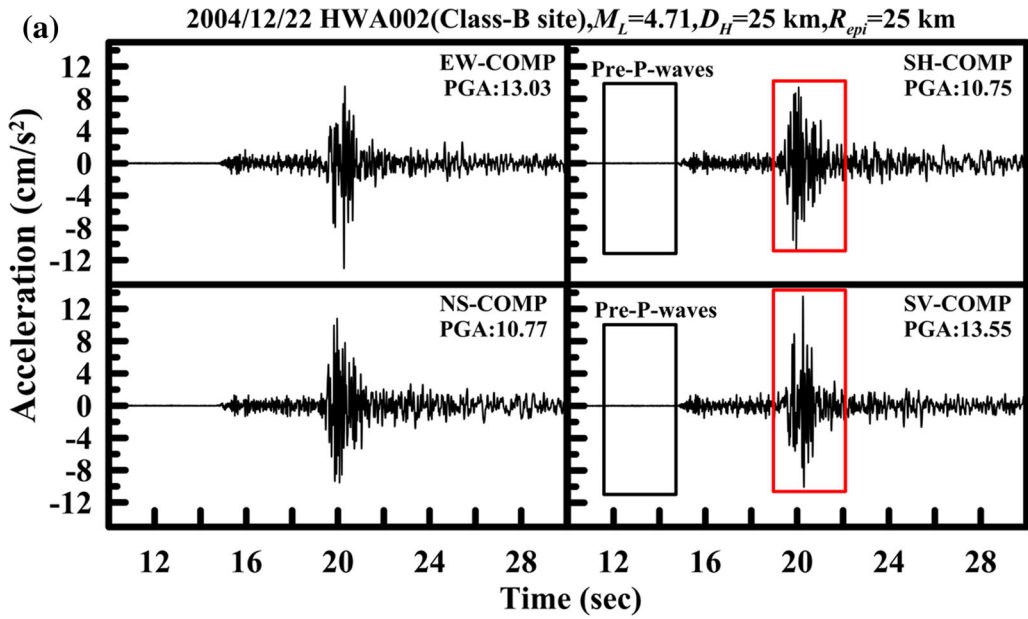
Hanks (1979, 1982) observed that acceleration spectral amplitudes are flattened at frequencies above  $f_c$ , and appear to be significantly attenuated above a certain frequency that falls between 10 and 20 Hz ( $f_{\max}$ ). In later work, Anderson and Hough (1984) found that  $f_E$  may fall below 5 Hz, and suggested that  $f_E$  is not limited to one band. Analysis of the high-cut process of accelerations from the Strong Motion Array in Taiwan, phase I (SMART 1) recordings in Lotung, revealed that  $f_E$  depends on both the site and on source effects (Tsai and Chen 2000).

Since  $f_E$  was manually and subjectively selected in this study, a sensitivity test was performed for each record. The  $f_E$  value is from 0.5 to 24 Hz, with an interval of 0.5 Hz. The  $f_X$  value is a fixed value. We use these different  $f_E$  values to calculate the  $\kappa_r$  values and pick the most appropriate  $f_E$  value. For example, we calculate the  $\kappa_r$  value of this seismic record. When the  $f_X$  is 32 Hz, and  $f_E$  increases from 0.5 to 24 Hz, the interval is 0.25 Hz. (See Fig. 3 for the fitting results and measured  $\kappa_r$  values against various  $f_E$ )

As shown in Fig. 3b, the dots in the figure are the  $\kappa_r$  values, and the lines show their standard errors. Firstly, we found that as the amplitude increases with frequency, the  $\kappa_r$  increases with  $f_E$  value ( $f_E < 4$  Hz) and standard errors are very large. When the amplitude begins to decrease,  $\kappa_r$ s decreases with  $f_E$  for  $4 < f_E \leq 8$  Hz, and the standard errors are still large. When the  $f_E$  value is 8.25 Hz, the standard deviation is 0.022, and the standard deviation at 8.5 Hz is 0.005, which is significantly smaller. The  $\kappa_r$  values are almost constant at frequencies of 8–18 Hz, which is about 0.056 s. After 18 Hz, the  $\kappa_r$  varies again, and the amounts of deviations are small. So the  $f_E$  value of this example is chosen to be 8.5 Hz. As the value of  $f_E$  increases, the value of  $\kappa_r$  also changes. Similar behavior was observed in Edwards et al. (2015) and Mayor et al. (2018). It is deduced that the selected  $f_E$  value should fall within the almost-constant range of the  $\kappa_r$  value change, so that  $\kappa_r$  can be obtained with a stable and reliable value. And the  $f_E$  value must be greater than the  $f_r$  value.

The National Earthquake Hazards Reduction Program (NEHRP) categorizes site conditions into the following five classes: class A (hard rock), class B (rock), class C (very dense soil and soft rock), class D (stiff soils), and class E (soft soils; BSSC 2001; Boore 2004; Holzer et al. 2005). Figure 4 shows the selected  $f_E$  versus  $M_L$  grouped according to  $R_{\text{epi}}$ , for four site classes (B to E) where there are enough recordings to perform a statistical analysis (at least 10 records). In addition, there were five groups according to  $R_{\text{epi}}$  taken into comparison: for  $R_{\text{epi}} < 30$  km, for  $R_{\text{epi}}$  in 30–59 km, for  $R_{\text{epi}}$  in 60–89 km, for  $R_{\text{epi}}$  in 90–119 km and, finally, for  $R_{\text{epi}} \geq 120$  km.

In general,  $f_E$  decreases with increasing  $M_L$  among these five groups. The  $f_E$  for  $R_{\text{epi}}$  in the range of 30 km was typically greater than the  $f_E$  associated



with other  $R_{epi}$  ranges, while  $f_E$  was smallest when  $R_{epi}$  was greater than 120 km. Although Fig. 4c shows that  $f_E$  values at different  $R_{epi}$  ranges were

similar, the effect of distance is nevertheless apparent. Therefore, we can conclude that distance and magnitude are factors that control  $f_E$ .

◀Figure 2

**a** An example accelerogram of the east–west (E-COMP), north–south (N-COMP), SH components (SH-COMP), and shear vertical (SV) components (SV-COMP) from the HWA002 station. The red rectangle represents the manual selection of the SH and SV wave. The black rectangle depicts background noise. **b** The corresponding Fourier amplitude spectrum. The regression line of the 50–100-Hz signal (red line) represents the background noise or the flat instrumental response. A selection of  $f_E$  and  $f_X$  used to compute  $\kappa$  directly from the SH and SV wave spectrum is shown in comparison with the noise spectrum of the record

4.2. Effect of Hypocentral Depth on  $\kappa_r$

The  $m_\kappa$  estimated from the subduction events for different stations was similar, and is mostly linked to regional attenuation properties (i.e., the  $Q$  factor). Because of different paths, the attenuation term may differ between crustal, intra-plate events and subduction, inter-plate events, which are generally associated with different hypocentral depths ( $D_H$ ;

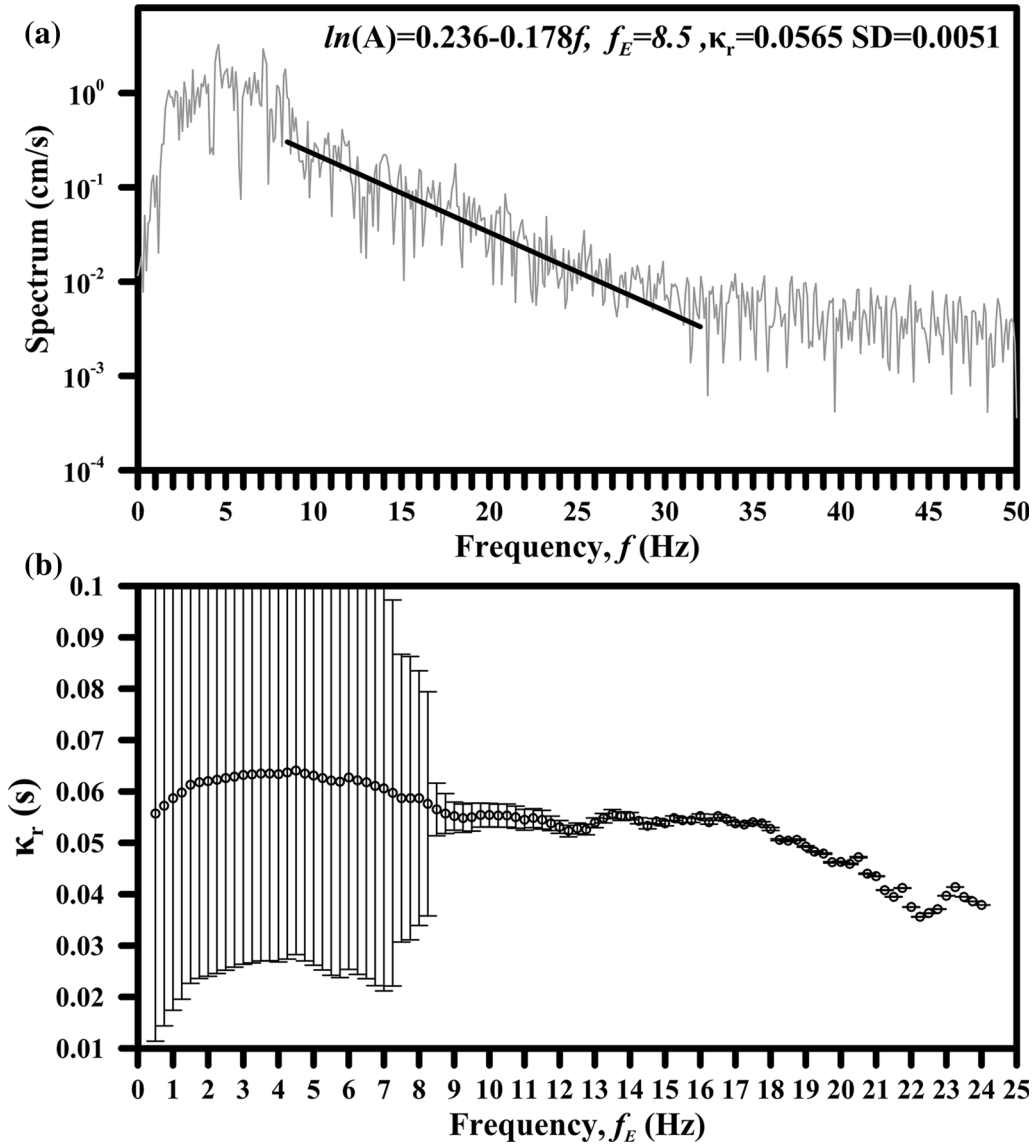


Figure 3

Spectral amplitudes for an example SH wave. The black solid lines in **a** show the least-squares fit with the frequency band. The circles in **b** show measured  $\kappa_r$  values against various  $f_E$  in the range of 0.5–24 Hz

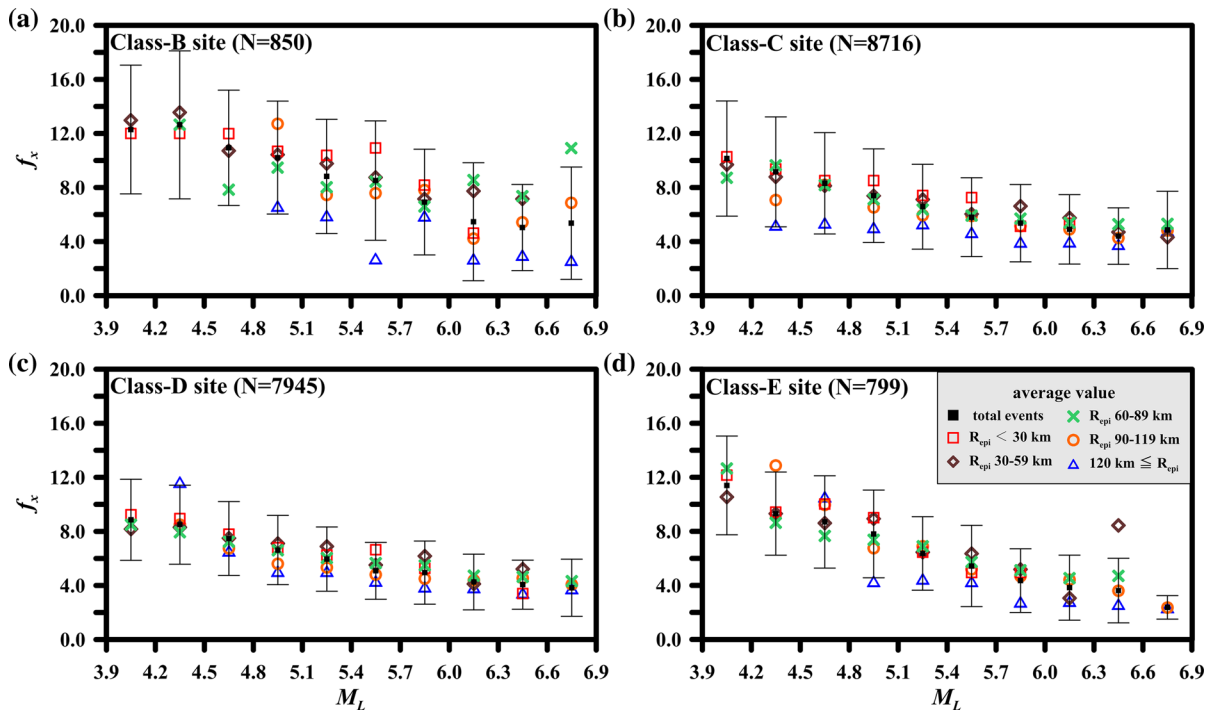


Figure 4

Estimated values of  $f_E$  plotted against magnitude ( $M_L$ ) for five  $R_{\text{epi}}$  groups at four site classes. The black squares and lines show the average  $f_E$  at equally spaced  $M_L$  bins and their standard errors, respectively. Five groups are distinguished based on  $R_{\text{epi}}$  (open square, diamond, cross, circle, and triangle), respectively corresponding to  $R_{\text{epi}} < 30$  km,  $R_{\text{epi}} 30\text{--}59$  km,  $R_{\text{epi}} 60\text{--}89$  km,  $R_{\text{epi}} 90\text{--}119$  km and  $R_{\text{epi}} \geq 120$  km, whereas the solid squares denote all events

Van Houtte et al. 2011). Figure 5 shows the measured  $\kappa_r$  against  $D_H$  for different site classes, where the crustal and subduction events are for  $D_H \leq 30$  km and  $D_H > 30$  km, respectively. The  $m_\kappa$  values are larger for crustal events than for subduction events, which implies that the anelastic effects of seismic wave lateral propagation are larger for crustal events (lower  $Q$  value) than for subduction events (larger  $Q$  value). Furthermore, in Fig. 5f, an example of station “ILA005,” the  $\kappa_r$ – $R_{\text{epi}}$  couples are categorized into three groups according to the hypocentral depths, i.e.,  $D_H < 30$  km,  $30 \leq D_H < 50$  km, and  $D_H \geq 50$  km.  $m_\kappa$ s from  $\kappa_r$ – $R_{\text{epi}}$  couples for  $30 \leq D_H < 50$  km and  $D_H \geq 50$  km are about the same, and are smaller than that for  $D_H < 30$  km.

Such attenuation differences result in significantly different  $\kappa_r$  values between crustal and subduction events for large epicentral distances ( $R_{\text{epi}} > 50$  km), whatever the site class (as shown in Fig. 5a for class-A site, HWA003; Fig. 5b for class-B site, TTN042;

Fig. 5c for class-C site, HWA051; Fig. 5d for class-D site, TCU079). In contrast,  $\kappa_r$  values for  $R_{\text{epi}}$  in the range of 10–50 km remain somewhat independent of the event type (crust or subduction), which may be caused by the regional attenuation. Assuming a simplified three-layer crustal model, the spectral decay factor can be given by Eq. 4 (Hough et al. 1988), as follows:

$$\kappa(R) = \frac{R_2}{\beta_2 Q_2} + \frac{R_1}{\beta_1 Q_1} + \kappa_0, \quad (4)$$

where  $R_1$ ,  $\beta_1$ , and  $Q_1$  are the thickness,  $S$  wave velocity, and quality factor of the layer 1, respectively, while  $R_2$ ,  $\beta_2$ , and  $Q_2$  are the thickness,  $S$  wave velocity, and quality factor of the layer 2.  $\beta_2$  and  $Q_2$  increase gradually with depth, given that  $R_2/\beta_2 Q_2$  has a smaller influence on  $\kappa_r$ , resulting in the  $\kappa_r$  values of subduction events that are very similar ( $\sim 30/\beta_1 Q_1 + \kappa_0$ ). Thus, measured  $\kappa_r$  values are about the same for crust and subduction events for  $R_{\text{epi}}$  in the



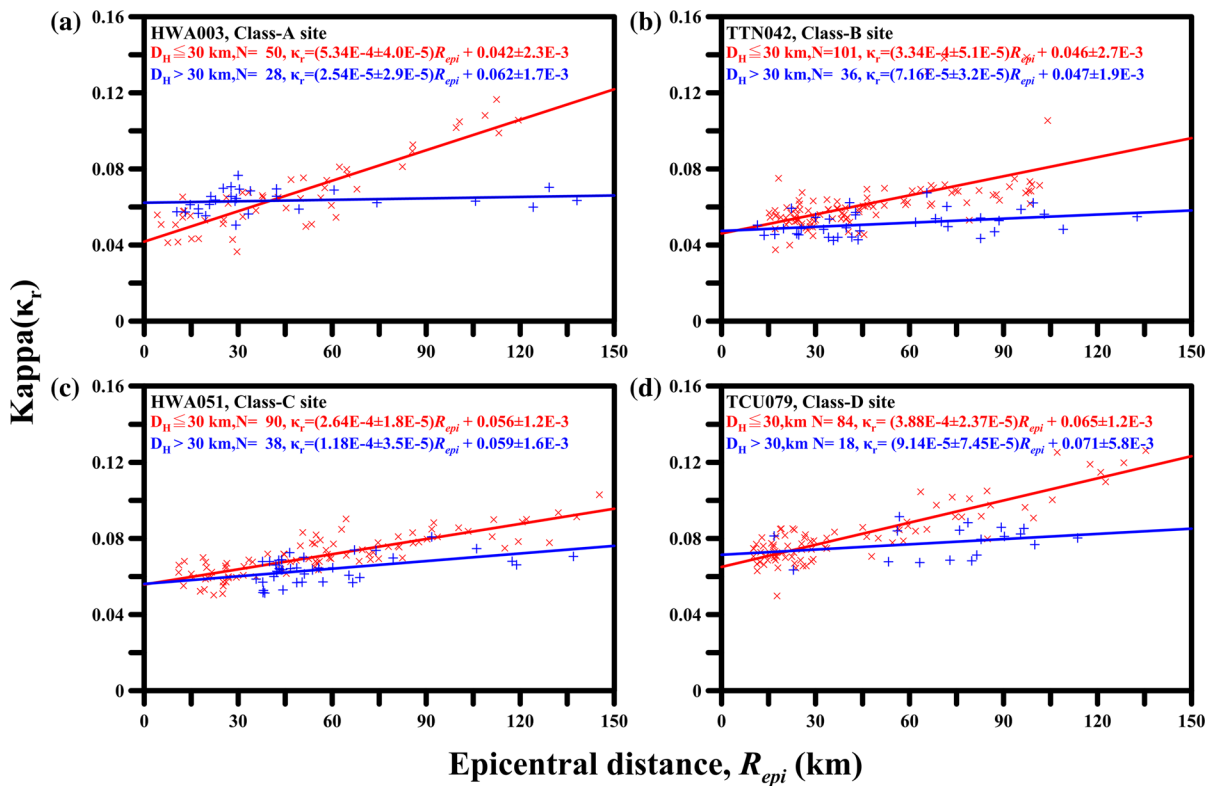


Figure 5

Comparison of different  $\kappa_r$  measurements against hypocentral depth,  $D_H$ , for example sites in each site class: **a** class-A (HWA003), **b** class-B (TTN042), **c** class-C (HWA051), **d** class-D (TCU079) sites. Equations for the fitted lines show  $D_H < 30$  km (red) and  $D_H > 30$  km (blue)

range of 10–50 km. If different regions of attenuation of the  $\kappa_r$  value were used for the regression, it would have affected the  $\kappa_0$  value; thus, we only used crustal events with  $D_H < 30$  km to estimate  $\kappa_r$ .

#### 4.3. Dependence of $\kappa$ on Source Back-Azimuth

The number and distribution of earthquake data points used may influence the regression. Figure 6 shows an example of station “CHY028” (denoted by a white triangle in the right-hand-side diagram) located in central Taiwan with various back azimuths with respect to earthquake sources with  $D_H \leq 30$  km, where the cross symbols in blue, red, and pink depict the earthquakes from the south, north, and southeast, respectively. The measured  $\kappa_r$ s of CHY028 station from earthquake events in the south, north and southeast are denoted by crosses, diamonds, and circles, respectively, along with linear fitting lines of

$\kappa_r$ – $R_{epi}$  couples. Although the  $\kappa_0$  values calculated for these three regions were highly similar and fell within the overall standard deviation of the mean of all data, the gradients obtained differed significantly. The  $\kappa_0$  value was mainly affected by the near-surface layers, and there was no obvious relationship with path. Waves from northern sources travel through the Central Mountain Range, which has a high  $Q_S$  (Wang et al. 2010), whereas waves from southern sources travel through the plains area, which have a relatively lower  $Q_S$ . The total attenuation due to  $Q_S$  and  $\kappa_0$  is then modelled as (Edwards et al. 2015):

$$\kappa_r = \frac{R}{Q_S \times \beta} + \kappa_0, \quad (5)$$

where  $\beta = 3.6$  km/s is the average shear wave velocity in the crust, and  $Q_S$  describes the  $S$  wave attenuation which is frequency-independent. From the  $\kappa_r$ – $R_{epi}$  couples, we can estimate  $\kappa_0$  and  $m_\kappa$  of the

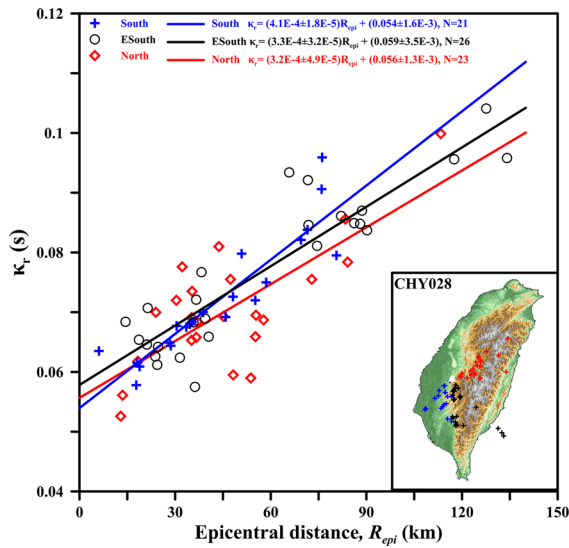


Figure 6

Sensitivity of  $\kappa_r$  to epicentral distance for one example station (CHY028) according to source back-azimuth for one in the south (blue lines and crosses), north (red lines and diamonds), and southeast (black lines and circles)

region, where  $1/(\beta \times Q_S)$  in Eq. 5 is equal to  $m_{\kappa}$ . Hence, we can compute  $Q_S$  by  $1/(\beta \times m_{\kappa})$ . The computed  $Q_S$  for earthquake source from the south, the south-east, and the north are 694 (636–765), 816 (751–896), and 925 (782–1134), respectively, where values in parentheses denote the standard deviation of  $Q_S$ . According to Eq. 5, lower  $Q_S$  will result in a higher slope. Clearly, regional geology will affect the slope. The  $Q_S$  values from the south are smaller than that from the north and the southeast, where the geology is recognized as stiff mountains/hills.

## 5. Results and Discussions

### 5.1. Relation of $\kappa_0$ with Geology

$\kappa_0$  values were computed by removing the regional anelastic effect for each station. Figure 7a shows the distribution of  $\kappa_0$  values plotted against topography. Since the number of TSMIP stations is large and dense, we map the  $\kappa_0$  value distribution (Fig. 7b). Consistent with expectation, the overall trend of  $\kappa_0$  is shown in Fig. 7b. The  $\kappa_0$  values below 0.06 s occurred in and around the Central Mountain Range and foothill areas, in the middle of Taiwan.

Conversely,  $\kappa_0$  values greater than 0.06 s were observed in the alluvial areas, i.e., the Taipei basin and the Ilan plain in northern Taiwan, the Chianan plain in the southwestern Taiwan, and the longitudinal valley in the eastern Taiwan. These areas have the higher values of  $\kappa_0$ . This may result from a bias in  $\kappa_r$  measurement for soft sites with resonance frequencies ( $f_r$ ) that fell in between the  $f_E$  and  $f_X$  (Parolai and Bindi 2004). In addition, for sites with  $\kappa_0$  values below 0.06 s, the correlation with topographical elevation was investigated. Our results confirm the clear relationship between  $\kappa_0$  and geology, as proposed by Ktenidou et al. (2015) who suggested that  $\kappa_0$  correlates with the site indicator,  $V_{S30}$ . Further details are given below.

$V_{S30}$  is frequently used to classify the site conditions under the NEHRP (BSSC 2001; Boore 2004; Holzer et al. 2005). Investigation of  $V_{S30}$  in Taiwan was conducted by the National Center for Research on Earthquake Engineering (NCREE) and the CWB during well logging for engineering applications from 2000 to 2012. There are 439 stations with  $V_{S30}$  (Kuo et al. 2012). The  $V_{S30}$  values at 385 stations with drilling depth of 30 m are computed as the averaged  $S$  wave velocity from the logging measurements (a suspension PS-logger system) which have a logging test every 0.5 m, whereas the rest (54 stations) with drilling depth less than 30 m are inferred using extrapolation technique (Kuo et al. 2011). Table 1 shows the average  $\kappa_0$  values estimated for the different site classes. For the 190 stations estimated as class-C sites, low  $\kappa_0$  values ( $< 0.045$ ) were obtained at 14 stations, and many of these stations are located at the edge of the Eastern Mountain (see Fig. 7). Furthermore, these low- $\kappa_0$  class-C sites have similar characteristics, with long and complex time-domain waveform signals. High frequencies have significant energy, and high  $f_X$  results in lower  $\kappa_r$ . It is possible that high-frequency signals are predominant at stations located at the perimeter of the Eastern Mountain that characterizes with less attenuation in the stiffer mountainous formation. Therefore, the results of these low- $\kappa_0$  class-C stations were not included in the empirical formula in Fig. 8, nor in the average  $\kappa_0$  values presented in Table 1.

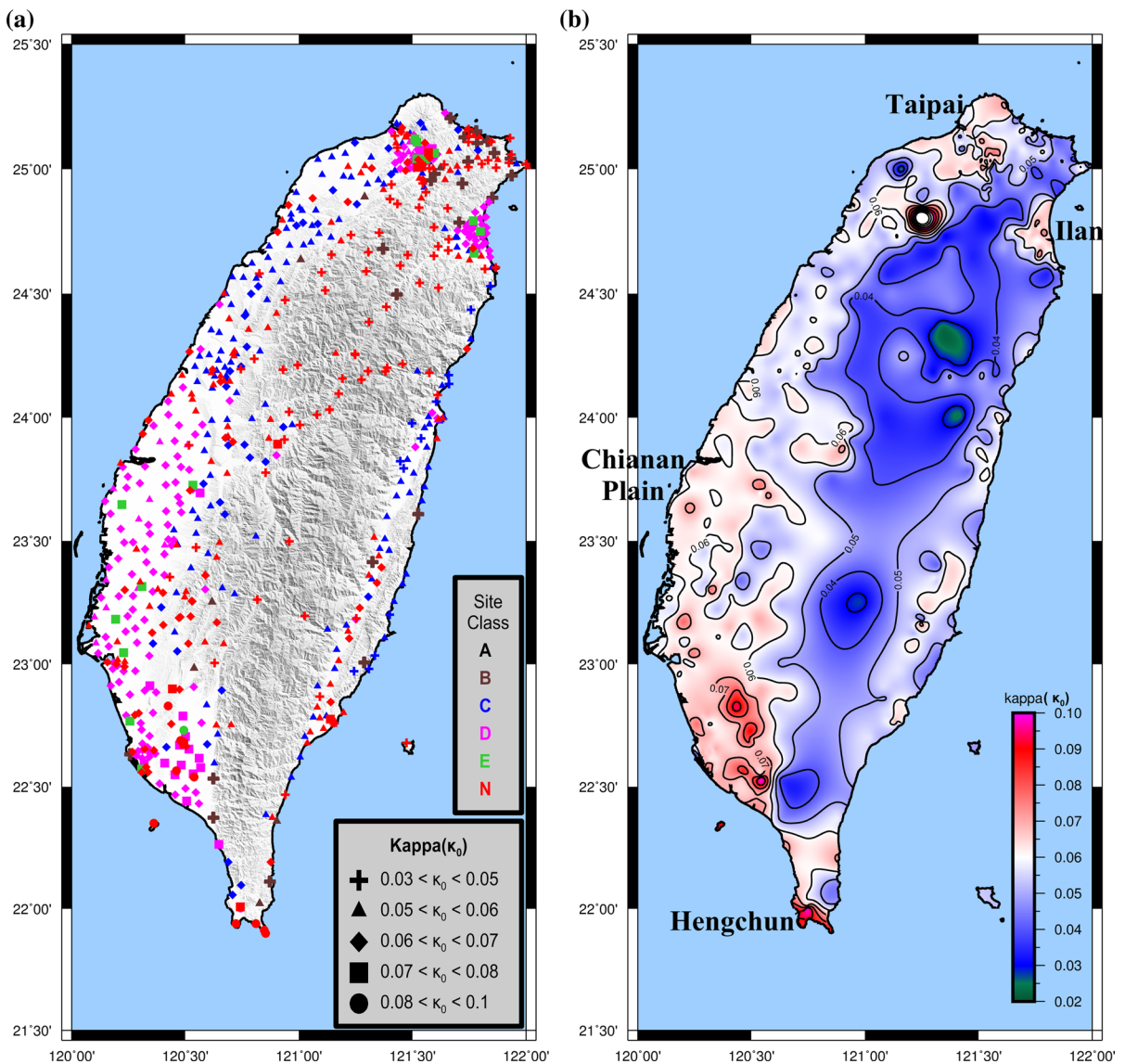


Figure 7

**a**  $\kappa_0$  map showing the results from 679 TSMIP stations. The different colors represent different site classes, and  $\kappa_0$  ranges are depicted by different symbols. **b** Contour map of  $\kappa_0$  across Taiwan

Figure 8 displays the  $\kappa_0$ - $V_{S30}$  couples. The relationship between  $\kappa_0$  and  $V_{S30}$  can be described by the following least-squares model:

$$\kappa_0 = (0.125 \pm 0.005) - (0.011 \pm 0.001) \times \ln(V_{S30}) \quad (6)$$

The squared correlation coefficient ( $R^2$ ) is 0.57. We compared the results of the present study with empirical correlations of  $\kappa_0$  and  $V_{S30}$  from the

following prior studies: Silva et al. (1998), who reported the relationship for  $V_{S30}$  above 300 m/s in California; Chandler et al. (2006), who compiled results from various areas (i.e. USA, Taiwan, Italy, and Japan) to generate the  $\kappa_0$ - $V_{S30}$  relationship for  $V_{S30}$  values greater than 500 m/s; Edwards et al. (2011), who investigated the relationships in Switzerland for  $V_{S30}$  above 400 m/s; and Van Houtte et al. (2011), who provided the relationship in Japanese

Table 1  
Average values of  $\kappa_0$  estimated for different class sites

Site class	$V_{S30}$ (m/s)	$\kappa_0$ (s)	$\sigma$ ( $\kappa_0$ ; s)	Nos.
A	> 1500	0.0418	–	1
B	760–1500	0.0469	0.0044	30
C	360–760	0.0564	0.0045	190
D	180–360	0.0643	0.0044	188
E	< 180	0.0744	0.0043	16
N	–	–	–	254

– No available data

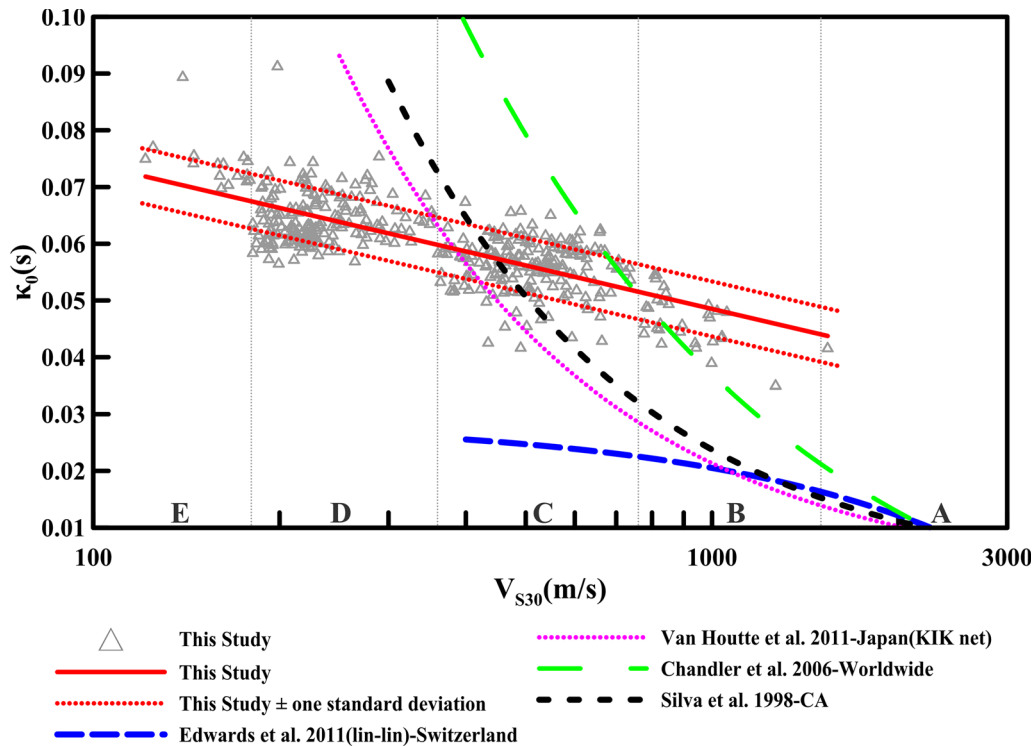


Figure 8

Plot of  $V_{S30}$  versus  $\kappa_0$  values (triangles) derived in this study, compared with the relationships between  $V_{S30}$  and  $\kappa_0$  values derived in previous studies. The red line is the regression line (Eq. 6), and red dotted line shows  $\pm$  one standard deviation

and the Next Generation Attenuation (NGA) data for  $V_{S30}$  values of 300–3000 m/s. These studies report low  $\kappa_0$  for high  $V_{S30}$  ( $\geq 1500$  m/s), but in lack of  $\kappa_0$  for  $V_{S30} \leq 360$  m/s. Therefore, the existing empirical formula of the  $\kappa_0$ – $V_{S30}$  relationship is poorly verified for the site condition of  $V_{S30} \leq 360$  m/s. In contrast, in the present study, we incorporate a large number of class-D and class-E stations to compute  $\kappa_0$ , but still

lacked analysis of class-A stations for comparison. As a result, the proposed formula of the  $\kappa_0$ – $V_{S30}$  relationship is well verified for the low- $V_{S30}$  area, but poorly verified for the  $V_{S30} > 1500$  m/s areas. Although, the  $\kappa_0$ – $V_{S30}$  relationships proposed by Silva et al. (1998), Chandler et al. (2006), Edwards et al. (2011), and Van Houtte et al. (2011) are different and do not span the same  $V_{S30}$  ranges, it can

be concluded that  $\kappa_0$  decreases with increasing  $V_{S30}$ . And results in this study are consistent with the latest results (Ktenidou et al. 2016, 2017; Laurendeau et al. 2016), which suggest much higher values than previously expected for rock and hard-rock sites. As well, Ktenidou et al. (2014) stated that the differences among the existing  $\kappa_0$ - $V_{S30}$  correlations are due to the regions, the methods, and the selected ranges of frequency.

Figure 9a, b shows the correlation between station  $\kappa_0$  values and  $V_{S30}$  from different class-C and class-D regions, respectively. The  $\kappa_0$  from the

forementioned seven geographical areas belonging to the same site class are mostly concentrated within a small range (e.g. the averaged  $\kappa_0$  of class-C sites varied from 0.05 to 0.06 s in Fig. 9c, and the averaged  $\kappa_0$  of class-D sites varied from 0.06 to 0.07 s in Fig. 9d), and  $\kappa_0$  and  $V_{S30}$  are not necessarily related. Most class-C stations are located on hills or hillsides, where large lateral variation in subsurface structures may occur. As a result, the distribution of  $\kappa_0$  values from stations in the same geographical area appears scattered (e.g. TCU, Fig. 9a). The averaged  $\kappa_0$  values with one standard deviation for the different

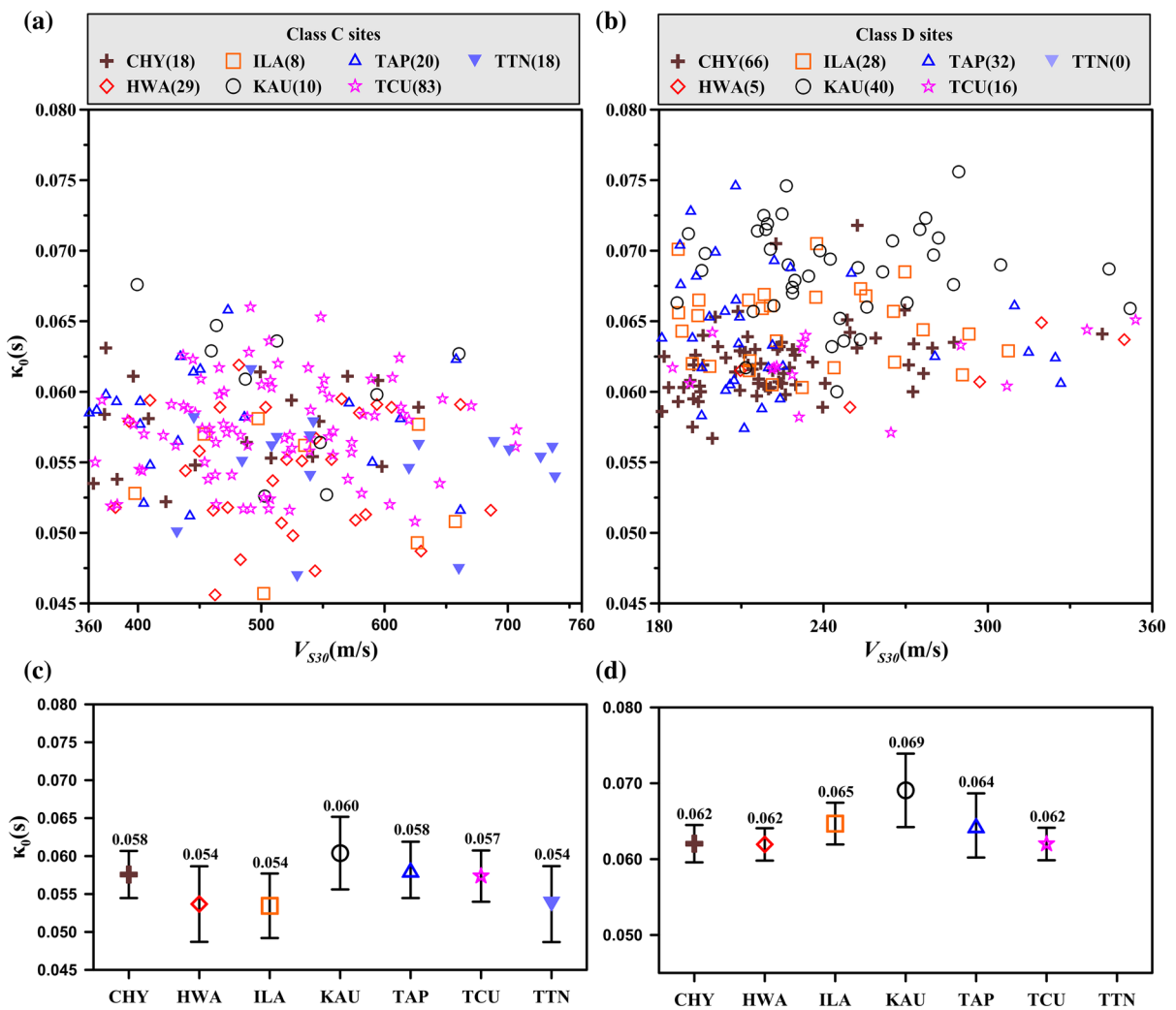


Figure 9

Correlation of  $\kappa_0$  values with  $V_{S30}$  from **a** class-C and **b** class-D sites. **c**, **d** Respectively show the average  $\kappa_0$  values of different regions, and black line shows  $\pm$  one standard deviation

geographical zones are listed in Table 2. In contrast, the distribution of  $\kappa_0$  values from class-D stations is narrow (Fig. 9b). The CHY station group has 66 stations, of which 61 have  $\kappa_0$  ranges from 0.058 to 0.065 s, with an average of  $0.062 \pm 0.0015$  s. The TCU station group has 16 stations, which includes 15 stations with  $\kappa_0$  ranging from 0.058 to 0.065 s, and an average of  $0.062 \pm 0.0019$  s. The class-D stations of the TCU and CHY stations are located on the north and south of the Chianan plain in southwestern Taiwan, and have similar  $\kappa_0$  values. Lin et al. (2009) depicted the  $S$  wave velocity for the western coastal plain of Taiwan utilizing independent seismic data from the microtremor array. They stated that unconsolidated sediments with thickness of less than 750 m are distributed underneath the Chianan Plain. And this may play an import role on the similarities in  $\kappa_0$ . These results indicate that  $\kappa_0$  values do not fluctuate significantly between regions with a similar shallow structure. The KAU station group has 40 stations, which includes 19 stations with  $\kappa_0$  ranging from 0.065 to 0.075 s, an average of 0.069 with a standard deviation of 0.0024 s, and  $V_{S30}$  ranging from 186 to 351 m/s. These stations are located on the Pingtung Plain, where thickness of the recent alluvial layer is 29–73 m (Chiang 1971). Below that depth, the formation is Linkou Conglomerate, a conglomerate inclusion with a thin layer of sandstone. Thus, in this area,  $V_{S30}$  only represents the velocity of modern alluvium, but cannot represent the deeper formation velocity.

## 5.2. Correlation of $\kappa_0$ with Other Site Parameters (Sediment Thickness, Elevation, and Resonance Frequencies)

Since the site-specific  $\kappa_0$  values are computed around the Taiwan area, we continue to investigate the correlation between those and other site proxies, i.e., the sediment thickness, elevation, and resonance frequency. The details are as follows. Firstly, Liu et al. (1994) found that  $\kappa_0$  values were dependent on sediment thickness in the upper Mississippi Embayment. Campbell (2009) also showed that  $\kappa_0$  values are dependent on the sediment thickness for the soft sites. The depth to engineering rock ( $V_s=1.0$  km/s), which is denoted as  $Z_{1.0}$ , is taken into investigation with  $\kappa_0$ .  $Z_{1.0}$  is used in GMPEs for the site correction at a specific station (Abrahamson and Silva 2008). As shown in Fig. 10, there are 34 stations with  $Z_{1.0}$  from drilling hole logging measurement (Kuo et al. 2012), whereas 41 and 505 stations with  $Z_{1.0}$  inferred from microtremor array measurement are from Kuo et al. (2016) and Lin et al. (2009), respectively. The color pattern represents  $Z_{1.0}$  obtained from different site classes. Although the distribution of  $\kappa_0$  and  $Z_{1.0}$  is a discrete phenomenon, we attempt to find out the relationship between  $\kappa_0$  and  $Z_{1.0}$ . The black line is the regression obtained by the least-squares method, and the correlation coefficient ( $R^2$ ) of the regression equation is 0.3, where  $Z_{1.0}$  is in meters. This indicates that  $\kappa_0$  is a weak correlation with the measured value of  $Z_{1.0}$ , but  $\kappa_0$  still varies with the sediment thickness.

Table 2

The averaged  $\kappa_0$  and one standard deviation for the class-C and class-D sites in different geographical areas

	Class-C site			Class-D site		
	$\kappa_0$ (s)	$\sigma$ ( $\kappa_0$ ) (s)	Nos.	$\kappa_0$ (s)	$\sigma$ ( $\kappa_0$ ) (s)	Nos.
CHY	0.058	0.0031	18	0.062	0.0025	67
HWA	0.054	0.0050	31	0.062	0.0021	5
ILA	0.054	0.0043	8	0.065	0.0027	29
KAU	0.060	0.0048	10	0.069	0.0048	42
TAP	0.058	0.0037	20	0.064	0.0042	32
TCU	0.057	0.0034	83	0.062	0.0021	16
TTN	0.054	0.0050	20	–	–	–

Site classes after Kuo et al. (2012)

– No available data

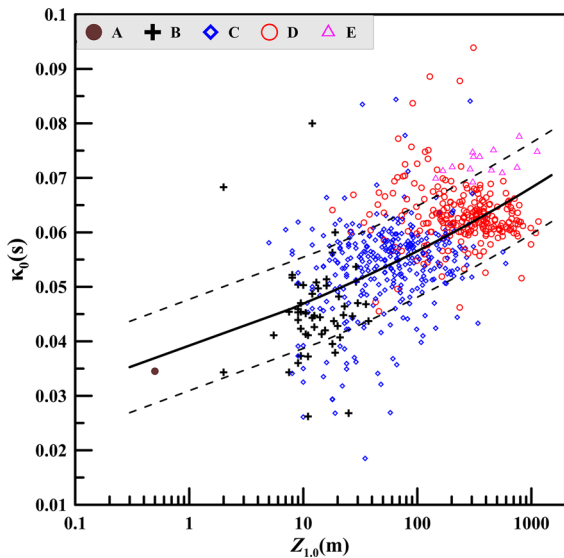


Figure 10

Correlation of the  $Z_{1,0}$  and  $\kappa_0$  values. Color patterns represent  $Z_{1,0}$  obtained from different site classes. The black line is the regression line, and black dotted line shows  $\pm$  one standard deviation

In addition, Fu and Li (2016) observed that  $\kappa_0$  decreases as elevation increases, and suggested that a regional  $\kappa_0$  model may also be developed from this correlation. Moreover, high-elevation geological drilling is not typically conducted in Taiwan. At altitudes above 500 m, there are 69 stations, but only 11 of these have drilling data, and the remaining stations are classified by Kwok et al. (2017). Figure 11 shows  $\kappa_0$  values from TSMIP stations against elevations above 100 m. Figure 11a icons are classified according to  $Z_{1,0}$  value, and (b) icons are classified according to site class. The three colored lines depict, respectively, the  $\kappa_0$ - $h$  relations of Gentili and Franceschina (2011) in red for Alps and Dinarides with  $R^2 = 0.26$ , Kilb et al. (2012) in blue for southern California with  $R^2 = 0.60$ , and Fu and Li (2016) in green for the Longmenshan area, China, with  $R^2 = 0.41$ .

In Fig. 11a, the black circles represent  $Z_{1,0} \leq 20$  m, the green crosses represent  $20 \leq Z_{1,0} \leq 40$  m, and the blue rectangles represent  $40 \leq Z_{1,0} \leq 140$  m. The black, red, and blue lines, respectively, show the best-fit relationship at different  $Z_{1,0}$  intervals. The stations with deeper sediment thickness (larger  $Z_{1,0}$ ) in a mountainous area will have larger

$\kappa_0$ , and the positive correlation relation was found in this figure. Generally, in a mountainous region, kappa values were smaller at those stations having shallower sedimentary layers (smaller  $Z_{1,0}$ ), which implies that high-frequency behaviors were controlled by the whole soil structure, not the top-most 30 m only. Therefore, the  $\kappa_0$ - $h$  correlation of each interval is not high, but there is still a clear trend for sediment thickness.

In Fig. 11b, the black circles represent class-B sites, the green crosses represent class-C sites, and the blue rectangles represent class-D sites. The overall trend is similar in the three areas with various gradients, showing that  $\kappa_0$  decreases with increasing  $h$ . The black dotted line is the regression of B site data ( $R^2 = 0.40$ ), and this line is similar to the result of Kilb et al. (2012). Since most of the data is class-C stations, and most of the class-C stations are located on hills or hillsides, the elevations are more variable. The reason for the discrepancy may be that the stations in the mountainous areas of Taiwan are not generally built on rock sites, but on mountain plains. The mountain plains may have an alluvial layer on the surface. For example, this is the case for CHY074, which is located at an altitude of 2413 meters.  $V_{S30}$  is 524.61 m/s for class-C stations, and the local  $\kappa_0$  value is 0.060 s, a disparity that derives from the station being built in a non-rock site within rocky terrain.

Finally, the correlation between  $\kappa_0$  and resonant frequency ( $f_r$ ) is determined in Taiwan from 416 TSMIP stations in order to verify  $\kappa_0$  with site-effect-related issues (Fig. 12). In this study, the  $f_r$  values are resonant frequency that have been measured using the average horizontal-to-vertical spectral ratio (HVSr) of the microtremor measurement (Huang 2009). In general, HVSr is correlated with geological conditions of topmost layers; the  $f_r (= V_S/4H; H$  means thickness) indicates where the main site response occurs and are highly correlated with the thickness of topmost sediment which lie on base rock (Huang et al. 2017). The black line in Fig. 12 displays the least-squared fitting of both logarithmic axes given a slope of  $-0.092$ , which implies a slight correlation between  $\kappa_0$  and  $f_r$ , given by the following equation:

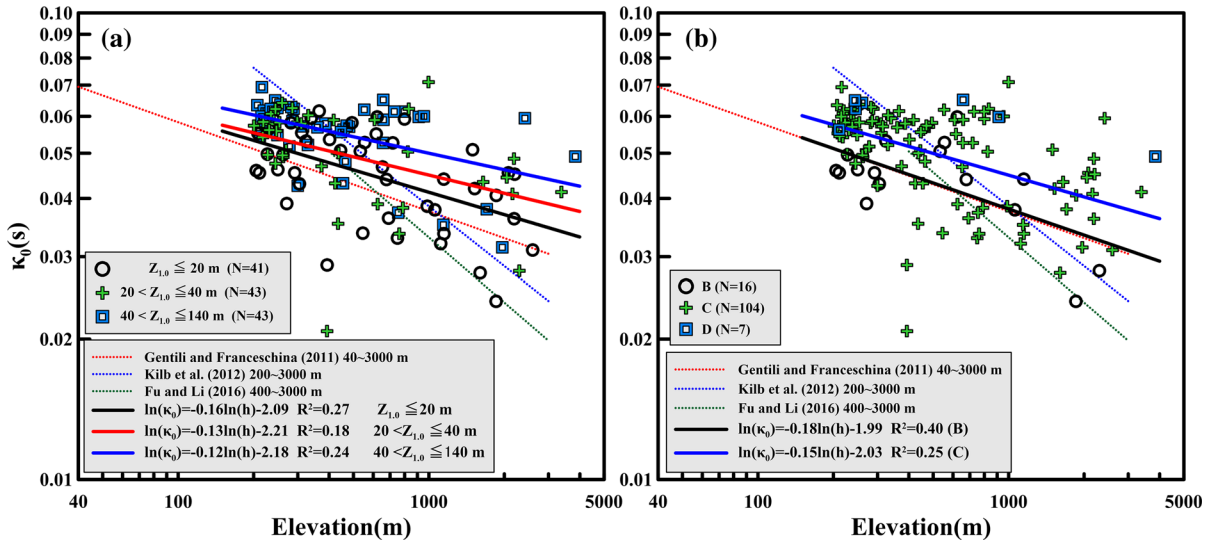


Figure 11

Correlation between elevation and  $\kappa_0$ . Symbols represent the individual  $\kappa_0$  values from TSMIP stations with elevations larger than 200 m. The dotted lines in red, blue, and green, respectively, show the  $\kappa_0$ - $h$  relations of Gentili and Franceschina (2011) for Alps and Dinarides, Kilb et al. (2012) for southern California, and Fu and Li (2016) for the Longmenshan area, China. **a** Classification by  $Z_{1,0}$  value. The black, red, and blue lines, respectively, show the best-fit relationship at different  $Z_{1,0}$  intervals. **b** Classification by site class. The black and blue lines, respectively, show the best-fit relationship at class-B and class-C site

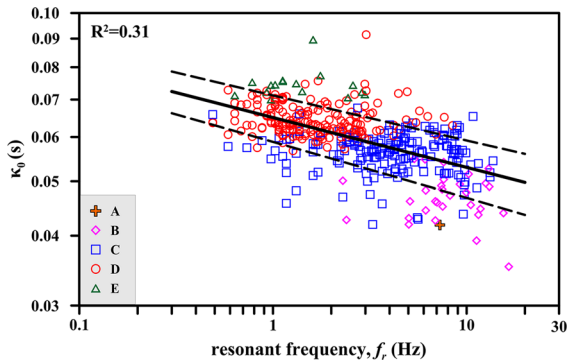


Figure 12

The relation between the estimated  $\kappa_0$  values and the resonant frequency obtained from HVSRS of earthquake data surveyed in Taiwan. The crosses, diamonds, squares, circles, and triangles represent, respectively, class-A, class-B, class-C, class-D, and class-E sites based on  $V_{S30}$

$$\ln(\kappa_0) = (-2.733 \pm 0.1) - (0.089 \pm 0.008) \times \ln(f_r) \quad (7)$$

The  $R^2$  of Eq. 7 is 0.31. And the  $\kappa_0$ - $f_r$  relation is similar to that of Van Houtte et al. (2011), Ktenidou et al. (2015), and Huang et al. (2017).

### 6. Conclusions

$\kappa_0$  characterizes the attenuation relation at high frequency that is highly correspondent to the site effect and which can be applied to common application in engineering seismology, such as for GMPEs and for stochastic ground motion simulation. Traditionally, GMPEs are a function of source, path, and site terms. For the site terms,  $V_{S30}$  and depth parameters ( $Z_{1,0}$ ) mainly describe characteristic of shallow velocity structure. Therefore,  $V_{S30}$  does not explicitly include site response, especially for sedimentary layers that are more than 30 m deep (Castellaro et al. 2008; Lee and Trifunac 2010), and thus does not fully represent differences in the high-frequency spectrum. In practice, the specific  $\kappa_0$  for two kinds of GMPEs would be utilized to deal with the host-to-target adjustment issue and to accurately estimate the hazard for high-frequency ground motion (Al Atik et al. 2014; Bora et al. 2015 Laurendeau et al. 2013, 2018).  $\kappa_0$  obtained in this study has provided important information not only for stochastic simulation of specific location, but the results of the simulation can be used for the use of GMPE adjustments. Meanwhile, Taiwan has a large



and well-equipped network of geological stations that produce a high volume of good-quality seismic recordings; therefore, Taiwanese data are well suited for the analysis of  $\kappa_0$  values.

In this study, the Anderson and Hough (1984) model was used to estimate the  $\kappa$  and  $\kappa_0$  values of each TSMIP station, based on 26,277 SH component recordings from 679 stations, consisting of 2204 earthquakes with  $M_L$  4.0–7.0 in Taiwan. Tsai and Chen (2000) reported that both site and source effects control  $f_E$ . In this study,  $f_E$  was manually and subjectively selected from the acceleration spectrum. We observed that  $f_E$  decreased as either magnitude or  $R_{\text{epi}}$  increased, and thus concluded that  $R_{\text{epi}}$  also affects  $f_E$ . The hypocentral distance ( $D_H$ ) and back-azimuth of the epicenters could similarly affect  $\kappa_0$ , especially the slope. Nevertheless, the  $\kappa_0$  values obtained from different orientations were within one standard deviation of the overall mean of all data.

Finally, this study developed a  $\kappa_0$  map of Taiwan. The  $\kappa_0$  values of the TSMIP stations range from 0.0208 to 0.147 s, and correlate reasonably well with  $V_{S30}$ . The  $\kappa_0$  of stations in plains with similar regional geology are comparable, whereas the  $\kappa_0$  values of stations in hilly and basin areas fluctuate greatly. These differences in  $\kappa_0$  are primarily the result of near-surface structures, but we were unable to confirm the effects of depth in this study. We constructed a  $\kappa_0$ - $V_{S30}$  correlation model, the results of which can be used in the future application of GMPEs and simulation parameters. Also, the relationship between  $\kappa_0$  and the depth to engineering rock ( $Z_{1.0}$ ) is not well correlated, whereas that between  $\kappa_0$  and other site proxies (i.e., elevation and resonant frequency) present an acceptable correlation.

#### Acknowledgements

The authors would like to thank the Central Weather Bureau and the National Center for Research on Earthquake Engineering for providing the strong motion data. This work was funded by the Ministry of Science and Technology (MOST103-2625-M-008-017-MY3, MOST105-2116-M-008-012).

**Publisher's Note** Springer Nature remains neutral with regard to jurisdictional claims in published maps and institutional affiliations.

#### REFERENCES

- Abrahamson, N., & Silva, W. (2008). Summary of the Abrahamson & Silva NGA ground-motion relations. *Earthquake Spectra*, 24(1), 67–97. <https://doi.org/10.1193/1.2924360>.
- Al Atik, L., Kottke, A., Abrahamson, N., Hollenback, J., et al. (2014).  $\kappa$  ( $\kappa$ ) scaling of ground-motion prediction equations using an inverse random vibration theory approach. *Bulletin of the Seismological Society of America*, 104(1), 336–346. <https://doi.org/10.1785/0120120200>.
- Anderson, J. G., & Hough, S. E. (1984). A model for the shape of the Fourier amplitude spectrum of acceleration at high frequencies. *Bulletin of the Seismological Society of America*, 74(5), 1969–1993.
- Atkinson, G. M., & Boore, D. M. (2006). Earthquake ground-motion prediction equations for Eastern North America. *Bulletin of the Seismological Society of America*, 96(6), 2181–2205. <https://doi.org/10.1785/0120050245>.
- Baltay, A. S., & Hanks, T. C. (2014). Understanding the magnitude dependence of PGA and PGV in NGA-West2 data. *Bulletin of the Seismological Society of America*, 104(6), 2851–2865. <https://doi.org/10.1785/0120130283>.
- Beresnev, I. A., & Atkinson, G. M. (1997). Modeling finite-fault radiation from the  $\omega^n$  spectrum. *Bulletin of the Seismological Society of America*, 87(1), 67–84.
- Beresnev, I. A., & Atkinson, G. M. (1998). FINSIM—A FORTRAN program for simulating stochastic acceleration time histories from finite faults. *Seismological Research Letters*, 69(1), 27–32.
- Boore, D. M. (2003). Simulation of ground motion using the stochastic method. *Pure and Applied Geophysics*, 160, 635–676.
- Boore, D. M. (2004). Estimating  $V_{S(30)}$  (or NEHRP site classes) from shallow velocity models (Depths < 30 m). *Bulletin of the Seismological Society of America*, 94(2), 591–597.
- Boore, D. M., & Joyner, W. B. (1997). Site amplifications for generic rock sites. *Bulletin of the Seismological Society of America*, 87(2), 327–341.
- Bora, S. S., Scherbaum, F., Kuehn, N., Stafford, P., & Edwards, B. (2015). Development of a response spectral ground-motion prediction equation (GMPE) for seismic-hazard analysis from empirical Fourier spectral and duration models. *Bulletin of the Seismological Society of America*, 105(4), 2192–2218.
- Building Seismic Safety Council (BSSC). (2001). NEHRP recommended provisions for seismic regulations for new buildings and other structures, Part 1: Provisions, prepared by the Building Seismic Safety Council for the Federal Emergency Management Agency (Report FEMA 368), Washington, D.C., 2000 Edition.
- Campbell, K. W. (2003). Prediction of strong ground motion using the hybrid empirical method and its use in the development of ground motion (attenuation) relations in eastern North America. *Bulletin of the Seismological Society of America*, 93(3), 1012–1033.

- Campbell, K. W. (2009). Estimates of shear-wave  $Q$  and  $\kappa_0$  for unconsolidated and semiconsolidated sediments in eastern North America. *Bulletin of the Seismological Society of America*, 99(4), 2365–2392. <https://doi.org/10.1785/0120080116>.
- Castellaro, S., Mulargia, F., Rossi, P. L., et al. (2008).  $V_{S30}$ : Proxy for seismic amplification? *Seismological Research Letters*, 79(4), 540–543.
- Castro, R. R., & Avila-Barrientos, L. (2015). Estimation of the spectral parameter kappa in the region of the Gulf of California, Mexico. *Journal of Seismology*, 19, 809–829. <https://doi.org/10.1007/s10950-015-9496-x>.
- Chandler, A., Lam, N., Tsang, H., et al. (2006). Near-surface attenuation modelling based on rock shear-wave velocity profile. *Soil Dynamics and Earthquake Engineering*, 26(11), 1004–1014. <https://doi.org/10.1007/s10950-005-9006-7>.
- Chen, K. P., Wang, C. Y., Tsai, Y. B., Chang, W. Y., et al. (2013). A seismic structure study in the Kaoping area, southwestern Taiwan. *Bulletin of the Seismological Society of America*, 103, 306–316.
- Chiang, S. C. (1971). Seismic study of the Chaochou structure, Pingtung, Taiwan. *Petroleum Geology of Taiwan*, 8, 281–294.
- Cormier, V. F. (1982). The effect of attenuation on seismic body waves. *Bulletin of the Seismological Society of America*, 72(1), 169–200.
- Cotton, F., Scherbaum, F., Bommer, J. J., Bungum, H., et al. (2006). Criteria for selecting and adjusting ground-motion models for specific target regions: Application to Central Europe and rock sites. *Journal of Seismology*, 10, 137–156.
- Douglas, J., Bungum, H., Scherbaum, F., et al. (2006). Ground-motion prediction equations for southern Spain and southern Norway obtained using the composite model perspective. *Journal of Earthquake Engineering*, 10, 33–72.
- Douglas, J., Gehl, P., Bonilla, L. F., Gélis, C., et al. (2010). A  $\kappa$  model for mainland France. *Pure and Applied Geophysics*, 167, 1303–1315. <https://doi.org/10.1007/s00024-010-0146-5>.
- Edwards, B., Fäh, D., Giardini, D., et al. (2011). Attenuation of seismic shear wave energy in Switzerland. *Geophysical Journal International*, 185, 967–984. <https://doi.org/10.1111/j.1365-246X.2011.04987.x>.
- Edwards, B., Ktenidou, O. J., Cotton, F., Abrahamson, N., Van Houtte, C., Fäh, D., et al. (2015). Epistemic uncertainty and limitations of the  $\kappa_0$  model for near-surface attenuation at hard rock sites. *Geophysical Journal International*, 202, 1627–1645.
- Fu, L., & Li, X. J. (2016). The characteristics of high-frequency attenuation of shear waves in the Longmen Shan and Adjacent Regions. *Bulletin of the Seismological Society of America*, 106(5), 1979–1990. <https://doi.org/10.1785/0120160002>.
- Gentili, S., & Franceschina, G. (2011). High frequency attenuation of shear waves in the southeastern Alps and northern Dinarides. *Geophysical Journal International*, 185(3), 1393–1416.
- Graves, R. W., & Pitarka, A. (2010). Broadband ground-motion simulation using a hybrid approach. *Bulletin of the Seismological Society of America*, 100(5A), 2095–2123. <https://doi.org/10.1785/0120100057>.
- Hanks, T. C. (1979).  $b$ -values and  $\omega^{-\gamma}$  seismic source models: implications for tectonic stress variations along active crustal fault zones and the estimation of high-frequency strong ground motion. *Journal of Geophysical Research*, 84, 2235–2242.
- Hanks, T. C. (1982).  $f_{\max}$ . *Bulletin of the Seismological Society of America*, 72(6A), 1867–1880.
- Hassani, B., & Atkinson, G. (2018). Adjustable generic ground-motion prediction equation based on equivalent point-source simulations: Accounting for Kappa effects. *Bulletin of the Seismological Society of America*, 108(2), 913–928. <https://doi.org/10.1785/0120170333>.
- Holzer, T. L., Padovani, A. C., Bennett, M. J., Noce, T. E., Tinsley, J. C., et al. (2005). Mapping NEHRP  $V_{S30}$  site classes. *Earthquake Spectra*, 21, 353–370.
- Hough, S. E., Anderson, J. G., Brune, J., Vernon, F., III, Berger, J., Fletcher, J., et al. (1988). Attenuation near Anza, California. *Bulletin of the Seismological Society of America*, 78(2), 672–691.
- Huang, J. Y. (2009). Using microtremor measurement to study the site effect in Taiwan area. Master thesis, National Central University (in Chinese with English abstract), p. 240.
- Huang, M. W., Wang, J. H., Hsieh, H. H., Wen, K. L., Ma, K. F., et al. (2005). Frequency-dependent sites amplifications evaluated from well-logging data in central Taiwan. *Geophysical Research Letters*, 32, L21302. <https://doi.org/10.1029/2005GL023527>.
- Huang, M. W., Wang, J. H., Ma, K. F., Wang, C. Y., Hung, J. H., Wen, K. L., et al. (2007). Frequency-dependent site amplifications with  $f \geq 0.01$  Hz evaluated from the velocity and density models in Central Taiwan. *Bulletin of the Seismological Society of America*, 97(2), 624–637. <https://doi.org/10.1785/0120060139>.
- Huang, M. W., Wen, K. L., Chang, S. C., Chang, C. L., Liu, S. Y., Chen, K. P., et al. (2017). The high-cut parameter (kappa) for the near-surface geology in and around the Taipei basin, Taiwan. *Bulletin of the Seismological Society of America*, 107(3), 1254–1264.
- Kilb, D., Biasi, G., Anderson, J. G., Brune, J., Peng, Z., Vernon, F. L., et al. (2012). A comparison of spectral parameter kappa from small and moderate earthquakes using southern California ANZA seismic network data. *Bulletin of the Seismological Society of America*, 102, 284–300.
- Ktenidou, O. J., Abrahamson, N., Drouet, S., Cotton, F., et al. (2015). Understanding the physics of kappa ( $\kappa$ ): Insights from a downhole array. *Geophysical Journal International*, 203, 678–691. <https://doi.org/10.1093/gji/ggv315>.
- Ktenidou, O. J., Abrahamson, N., Silva, W., Darragh, R., et al. (2016). A methodology for the estimation of kappa ( $\kappa$ ) for large datasets. Example application to rock sites in the NGA-East database. Pacific Earthquake Engineering Research Center, PEER report 2016/01, p. 117.
- Ktenidou, O. J., Cotton, F., Abrahamson, N., Anderson, J. G., et al. (2014). Taxonomy of kappa: A review of definitions and estimation approaches targeted to applications. *Seismological Research Letters*, 85, 135–146.
- Ktenidou, O. J., Silva, W., Darragh, R., Abrahamson, N., Kishida, T., et al. (2017). Squeezing kappa ( $\kappa$ ) out of the transportable array: A strategy for using bandlimited data in regions of sparse seismicity. *Bulletin of the Seismological Society of America*, 107(1), 256–275.
- Kuo, C. H., Chen, C. T., Lin, C. M., Wen, K. L., Huang, J. Y., Chang, S. C., et al. (2016). S-Wave velocity structure and site effect parameters derived by microtremor arrays in the western plain of Taiwan. *Journal of Asian Earth Sciences*, 128, 27–41. <https://doi.org/10.1016/j.jseaes.2016.07.012>.
- Kuo, C. H., Wen, K. L., Hsieh, H. H., Chang, T. M., Lin, C. M., Chen, C. T., et al. (2011). Evaluating empirical regression equations for  $V_s$  and estimating  $V_{S30}$  in northeastern Taiwan. *Soil*

- Dynamics and Earthquake Engineering*, 31, 431–439. <https://doi.org/10.1016/j.soildyn.2010.09.012>.
- Kuo, C. H., Wen, K. L., Hsieh, H. H., Lin, C. M., Chang, T. M., Kuo, K. W., et al. (2012). Site classification and  $V_{S30}$  estimation of free-field TSMIP stations using the logging data of EGD. *Engineering Geology*, 129–130, 68–75. <https://doi.org/10.1016/j.enggeo.2012.01.013>.
- Kwok, O. L. A., Stewart, J. P., Kwak, D. Y., Sun, P. L., et al. (2018). Taiwan-specific model for VS30 prediction considering between-proxy correlations. *Earthquake Spectra*, 34(4), 1973–1993.
- Lai, T. S., Mittal, H., Chao, W. A., Wu, Y. M., et al. (2016). A study on kappa value in Taiwan using borehole and surface seismic array. *Bulletin of the Seismological Society of America*, 106, 1509–1517.
- Laurendeau, A., Bard, P. Y., Hollender, F., Ktedinou, O. J., Foundotos, L., Hernandez, B., Perron, V., et al. (2016). Prediction of reference motions (1000\Vs3000 m/s) from corrected KiK-net records of the local site effects. In: 5th IASPEI/IAEE international symposium: effects of surface geology on seismic motion, August 15–17, Taipei.
- Laurendeau, A., Bard, P. Y., Hollender, F., Perron, V., Foundotos, L., Ktenidou, O. J., et al. (2018). Derivation of consistent hard rock ( $1000 < V_s < 3000$  m/s) GMPEs from surface and down-hole recordings: analysis of KiK-net data. *Bulletin of Earthquake Engineering*, 16(6), 2253–2284. <https://doi.org/10.1007/s10518-017-0142-6>.
- Laurendeau, A., Cotton, F., Ktenidou, O. J., Bonilla, L. F., Hollender, F., et al. (2013). Rock and stiff-soil site amplification: Dependency on  $V_{S30}$  and kappa ( $\kappa_0$ ). *Bulletin of the Seismological Society of America*, 103(6), 3131–3148. <https://doi.org/10.1785/0120130020>.
- Lay, T., & Wallace, T. C. (1995). *Modern global seismology* (p. 521). San Diego: Academic Press.
- Lee, V. W., & Trifunac, M. D. (2010). Should average shear-wave velocity in the top 30 m of soil be used to describe seismic amplification? *Soil Dynamics and Earthquake Engineering*, 30, 1250–1258.
- Lin, C. M., Chang, T. M., Wen, K. L., Huang, Y. C., Chiang, H. J., Kuo, C. H., et al. (2009). Shallow s-wave velocity structures in the western coastal plain of Taiwan. *Terrestrial, Atmospheric and Oceanic Sciences*, 20(2), 299–308. <https://doi.org/10.3319/TAO.2007.12.10.01>.
- Liu, Z., Wuenschel, M. E., Herrmann, R. B., et al. (1994). Attenuation of body waves in the central New Madrid seismic zone. *Bulletin of the Seismological Society of America*, 84(4), 1112–1122.
- Ma, K. F., Mori, J. M., Lee, S. J., Yu, S. B., et al. (2001). Spatial and temporal distribution of slip for the 1999 Chi-Chi, Taiwan, Earthquake. *Bulletin of the Seismological Society of America*, 91(5), 1069–1087.
- Mai, P. M., Imperatori, W., Olsen, K. B., et al. (2010). Hybrid broadband ground-motion simulations: combining long-period deterministic synthetics with high-frequency multiple S-to-S backscattering. *Bulletin of the Seismological Society of America*, 100(5), 2124–2142. <https://doi.org/10.1785/012008019>.
- Mayor, J., Bora, S. S., Cotton, F., et al. (2018). Capturing regional variations of hard-rock  $\kappa_0$  from coda analysis. *Bulletin of the Seismological Society of America*, 108(1), 399–408. <https://doi.org/10.1785/0120170153>.
- Parolai, S., & Bindi, D. (2004). Influence of soil-layer properties on  $\kappa$  evaluation. *Bulletin of the Seismological Society of America*, 94, 349–356.
- Shin, T. C., Chang, C. H., Pu, H. C., Lin, H. W., Leu, P. L., et al. (2013). The geophysical database management system in Taiwan. *Terrestrial, Atmospheric and Oceanic Sciences*, 24(1), 11–18. [https://doi.org/10.3319/TAO.2012.09.20.01\(T\)](https://doi.org/10.3319/TAO.2012.09.20.01(T)).
- Silva, W., Darragh, R., Gregor, N., Martin, G., Abrahamson, N., Kircher, C., et al. (1998). Reassessment of site coefficients and near-fault factors for building code provisions. Technical Report Program Element II: 98-HQGR-1010, Pacific Engineering and Analysis, El Cerrito, USA.
- Sokolov, V. Y., Loh, C. H., Wen, K. L., et al. (2004). Evaluation of generalized site response functions for typical soil classes (B, C, and D) in Taiwan. *Earthquake Spectra*, 20, 1279–1316.
- Toro, G. R., Abrahamson, N., Schneider, J. F., et al. (1997). Model of strong ground motions from earthquakes in central and eastern North America: Best estimates and uncertainties. *Seismological Research Letters*, 68, 41–57.
- Tsai, C. C. P., & Chen, K. C. (2000). A model for the high-cut process of strong-motion accelerations in terms of distance, magnitude, and site condition: An example from the SMART 1 Array, Lotung, Taiwan. *Bulletin of the Seismological Society of America*, 90(6), 1535–1542.
- Tsai, Y. B., Yu, T. M., Chao, H. L., Lee, C. P., et al. (2001). Spatial distribution and age dependence of human-fatality rates from the Chi-Chi, Taiwan, Earthquake of 21 September 1999. *Bulletin of the Seismological Society of America*, 91(5), 1298–1309.
- Van Houtte, C., Drouet, S., Cotton, F., et al. (2011). Analysis of the origins of  $\kappa$  (kappa) to compute hard rock to rock adjustment factors for GMPEs. *Bulletin of the Seismological Society of America*, 101(6), 2926–2941. <https://doi.org/10.1785/0120100345>.
- Van Houtte, C., Ktenidou, O. J., Larkin, T., Holden, C., et al. (2014). Hard-site  $\kappa_0$  (kappa) calculations for Christchurch, New Zealand, and comparison with local ground motion prediction models. *Bulletin of the Seismological Society of America*, 104(4), 1899–1913. <https://doi.org/10.1785/0120130271>.
- Wang, Y. J., Ma, K. F., Mouthereau, F., Eberhart-Phillips, D., et al. (2010). Three dimensional  $Q_p$ - and  $Q_s$ - tomography beneath Taiwan Orogenic Belt: Implication for tectonic and thermal structure. *Journal of Geophysical Research*, 180, 891–910. <https://doi.org/10.1111/j.1365-246X.2009.04459.x>.
- Wen, K. L., Chang, Y. W., Lin, C. M., Chiang, H. J., Huang, M. W., et al. (2008). Damage and ground motion of the 26 December 2006 Pingtung earthquakes, Taiwan. *Terrestrial, Atmospheric & Oceanic Sciences*, 19(6), 641–651. [https://doi.org/10.3319/TAO.2008.19.6.000\(PT\)](https://doi.org/10.3319/TAO.2008.19.6.000(PT)).
- Zandieh, A., Campbell, K. W., Pezeshk, S., et al. (2016). Estimation of  $\kappa_0$  implied by the high-frequency shape of the NGA-West2 ground motion prediction equations. *Bulletin of the Seismological Society of America*, 106(3), 1342–1356. <https://doi.org/10.1785/0120150356>.